Nano Energy 72 (2020) 104741

Contents lists available at ScienceDirect

Nano Energy

journal homepage: http://www.elsevier.com/locate/nanoen

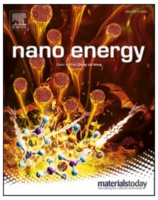

Functional integrated electromagnetic interference shielding in flexible micro-supercapacitors by cation-intercalation typed $Ti_3C_2T_x$ MXene

Xin Feng [a,b], Jing Ning [a,b,*], Boyu Wang [a,b], Haibin Guo [a,b], Maoyang Xia [a,b], Dong Wang [a,b], Jincheng Zhang [a,b], Zhong-Shuai Wu [c], Yue Hao [a,b]

[a] The State Key Discipline Laboratory of Wide Band Gap Semiconductor Technology, Xidian University, Xi'an, 710071, China
[b] Shaanxi Joint Key Laboratory of Graphene, Xidian University, Xi'an, 710071, China
[c] Dalian National Laboratory for Clean Energy, Dalian Institute of Chemical Physics, Chinese Academy of Sciences, 457 Zhongshan Road, Dalian, 116023, China

ARTICLE INFO

Keywords:
$Ti_3C_2T_x$ MXene
Cation intercalation
Density functional theory calculation
Micro-supercapacitors
Electromagnetic interference shielding

ABSTRACT

Multifunctional and flexible micro-supercapacitors (MSCs) have attractive prospects in integrated micro electronic systems fields owing to its high power density, fast charge/discharge rates and small volume feature. Here, a flexible MSC functional electromagnetic interference (EMI) shielding is designed based on Mn ion-intercalated $Ti_3C_2T_x$ MXene, presenting a high areal capacitance of 87 mF cm^{-2} at 2 mV s^{-1}, remarkable energy density of 11.8 mWh cm^{-3} and outstanding shielding effectiveness of 44 dB. By density functional theory (DFT) calculation, the interaction between Mn ions and surface terminal (-F, –O, and –OH) of $Ti_3C_2T_x$ is emphatically discussed, finding that the intercalated Mn ions are inclined to be bonding with O-contained groups with the orbital hybridization of Mn 3d and O 2p. It is intriguing to provide enhanced electrochemical performance in energy storage and additive interlayer EM waves absorption in EMI shielding. The present work can offer new insights about underlying mechanism of cation intercalation in $Ti_3C_2T_x$ MXene and multiple functional devices application in integrated micro electronics systems field.

1. Introduction

The development of portable, implantable, and wearable electronics miniaturized energy-storage devices has been an increasing demand in recent years since the rapid miniaturization of electronic gadgets, such as portable/wearable apparatuses, wireless micro-electro mechanical system (MEMS) sensors, auto-powered systems, and implantable medical chips [1–7]. Micro-supercapacitors (MSCs) have become a potential energy supply for constructing on-chip electronic systems by virtue of its high-power density [8–12]. Integrating MSCs with these electronic devices onto a single flexible substrate can potentially increase the package density and reduce the complexity of the overall system design. Despite significant progresses have been achieved in integrated systems for MSCs, a comprehensive review covering all aspects from system design principles, layout arrangement of components and signal responses to self-powered integrated systems has not yet been described so far. In fact, a failure of electronic devices and systems can be caused by the electromagnetic interference (EMI) radiated from the neighboring microwave circuits or radio-frequency circuits [13–15]. It's vitally important to control the electromagnetic pollution and require suitable protection for microwave shielding to keep the normal operation of electronics devices. In this regard, integrated MSCs are more suitable in multifunction with EM protection because of the simple in-plane architecture. The introduction of shielding functions into MSCs can save spaces in such a micro scale system, leading to a high space-utilization efficiency and package density.

Two-dimensional (2D) metal carbides/nitrides (MXenes) have emerged as a burgeoning group of layer-structure materials with a general chemical composition of $M_{n+1}X_nT_x$, where M represents an early transition metal, X indicates C and/or N, and T_x denotes to surface functional groups (-F, –O, and –OH) [16–20]. Among them, $Ti_3C_2T_x$ MXene is widely acknowledged as the most commonly used and promising active material for supercapacitors and MSCs [20–22], owing to its extraordinary physical and chemical properties, such as superb intrinsic electrical conductivity, tunable surface chemistry (various functional groups, e.g., –O, –OH and –F), and tunable layer structure [23–25]. Besides their application in energy storage, $Ti_3C_2T_x$ MXenes also exhibit particular characteristic in electromagnetic shielding because its high

---

* Corresponding author. The State Key Discipline Laboratory of Wide Band Gap Semiconductor Technology, Xidian University, Xi'an, 710071, China.
E-mail address: ningj@xidian.edu.cn (J. Ning).

https://doi.org/10.1016/j.nanoen.2020.104741
Received 28 January 2020; Received in revised form 23 March 2020; Accepted 24 March 2020

electrical conductivity contribute to the electromagnetic (EM) waves reflection [26–28]. Therefore, $Ti_3C_2T_x$ MXenes is a kind of optical materials to design and realize a multifunctional device used in the complex integrated system.

Although $Ti_3C_2T_x$ display higher capacitance as supercapacitor electrodes when compared to other carbon materials, their self-pseudocapacitance can be further improved by solving problems of the low accessible surface area and poor processability due to restacking [29]. Particularly, ion intercalation and interspace engineering are the effective strategies used to obtain enhanced pseudocapacitance [30,31]. Several studies have reported the ions intercalation strategy to enlarge the interlayer spacing, increase electrolyte accessibility, and improve ion transport [30,32,33]. Importantly, the surface terminals of $Ti_3C_2T_x$ play a critical role in the ion intercalation considering physical/chemical adsorption and chemical reaction [34,35]. Naguib et al. [36] reported that metal cations were adsorbed by electrostatic interaction due to negatively the charged groups on the surface. Wang et al. [37] presented a more stable structure of Co ions intercalated V_2C due to the formation of strong V–O–Co bonding. In this regard, the basic interaction between inserted ions and surface groups of MXene is vital

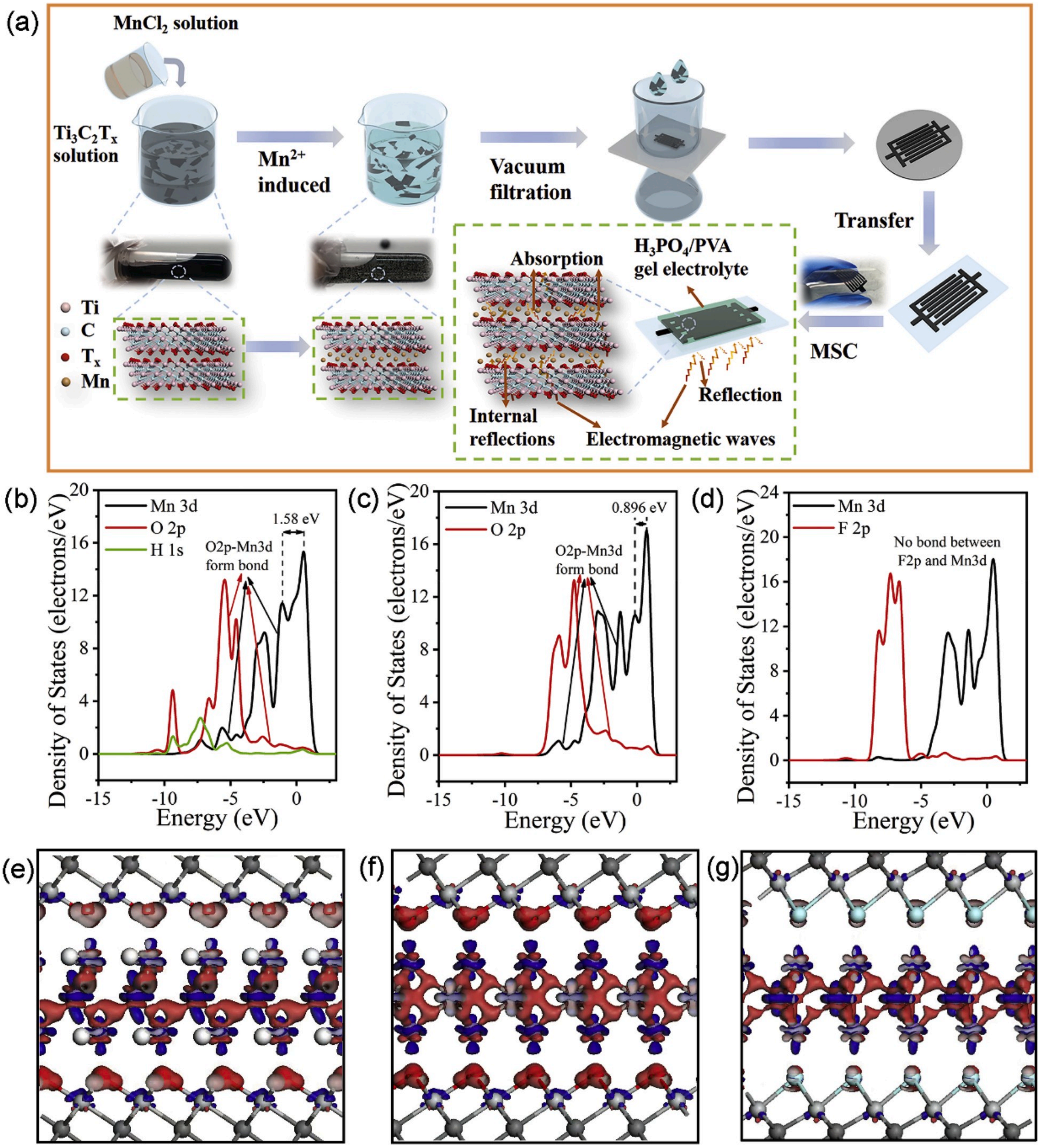

Fig. 1. (a) Schematic of the fabrication process of the MIT-based MSCs. Calculated PDOS for Mn ions and $Ti_3C_2T_x$. (T: OH, –O, –F) (b) With T = –OH, the orbitals of Mn3d, O2p and H1s, (c) With T = –O, the orbitals of Mn3d and O2p, (d) With T = –F, the orbitals of Mn3d and F2p. The fermi level is set at 0 eV. Differential charge density of Mn ions introduced $Ti_3C_2T_x$ with different surface functional groups with an isosurface value of is 0.1 e Å $^{-3}$, where the red and blue colors represent the electron accumulation and depletion regions, respectively. (e) –OH, (f) –O, (g) –F. Key: intercalant, Mn; red, O; white, H; cyan, F; gray, Ti; black, C.

for deeply understanding the advantage of ions intercalation for improving the ability of energy storage. Mn-based materials have been widely studied as the rapid redox reaction centers in cathode materials to boost the specific capacity [38]. Besides, the introduction of Mn is also supposed to form of interfacial heterojunctions to improve the conductivity and adsorption [39].

Herein, in this work, cation intercalation of transition metal Mn^{2+} ions into $Ti_3C_2T_x$ was proposed to enhance the ability of energy storage and EMI shielding. By density functional theory (DFT) simulation, the interaction mechanism between cation and surface functional groups was explored. It was found that the Mn ions were inclined to be bonding with oxygen-contained terminal by the orbital hybridization between Mn 3d and O 2p. Consequently, the bonding formation inspired the enhancement of electrical conductivity, additive pseudocapacitance and stability improvement. The Mn ions-introduced $Ti_3C_2T_x$ (hereinafter called as MIT) based MSCs exhibited an improved areal capacitance of 87 mF cm^{-2} and high volumetric energy density of 11.8 mWh cm^{-3}. Moreover, the MIT films display superior shielding efficiency of 42 dB, due to the multireflection and additive interface absorption of incident EM waves.

2. Results and discussion

The overall fabrication process of $Ti_3C_2T_x$ films and flexible MSCs were schematically illustrated in Fig. 1. The $Ti_3C_2T_x$ nanosheets were synthesized by ultrasonic exfoliation of multilayered $Ti_3C_2T_x$ precursors, before which the delaminated $Ti_3C_2T_x$ bulks were obtained by selectively etching the Al layers from the Ti_3AlC_2 MAX phase with a mixed solution of HCl and LiF. The acidic-fluoride-containing solutions led to the charging of terminal functional groups (-OH, –O, and –F) on the surface of $Ti_3C_2T_x$ nanosheets, making them hydrophilic in nature with uniform dispersion in water, as shown in the left image of Fig. 1. Through the addition of the Mn^{2+} ions contained solution, the mixed $Ti_3C_2T_x$ aqueous solutions were observed to flocculate in the aqueous solution (right image of Fig. 1). Further, the suspension was easily filtered to form the planar thin-film micro-electrodes of MSCs with assistance of an interdigitated customized mask, and then the patterned microelectrodes were readily transferred to a flexible substrate, such as polyethylene terephthalate (PET).

To clearly determine the influence of induced Mn ions on the aqueous solution in change, and to explain the interaction mechanism between cation and surface functional groups, the binding energy, projected density of states (PDOS) and differential charge densities between the cation and surface functional groups (-OH, –O, –F) on $Ti_3C_2T_x$ were simulated using DFT method, which could capture the electronic structure and properties. The completed structural models of cation intercalation in $Ti_3C_2T_x$ were depicted in Fig. S1. It was clearly shown that terminal atoms occupied on the top sites of the centro-Ti atoms, which is in agreement with previous studies [40,41]. The PDOS of Mn ions and functional groups of $Ti_3C_2T_x$ exhibited metallic properties near the Fermi level (0 eV) in Fig. 1b–d. Fig. 1b clearly displayed that the peaks of O 2p orbital was dominant at the lower energy ranging from −6.24 to −3.9 eV and invisible at the high energy of −3.9–1.42 eV, while it was converse in Mn 3d orbital, indicating the formation of Mn–O bond. This behavior was similar to that observed in Fig. 1c, which also exhibited the existence of Mn–O bond. Moreover, the pseudogap of Mn 3d orbital (the two peaks astride fermi level) in Fig. 1b showed a larger difference of 1.58eV, indicating that Mn ions were inclined to be bonding with O atoms in $Ti_3C_2(OH)_x$. It can be attributed to the lowest work functions of –OH terminated $Ti_3C_2T_x$ [41,42]. The inexistence of orbital hybridization between Mn 3d and F 2p demonstrated the inactivity of –F terminal in Fig. 1c, because the resultant of –F terminal was not a stable configuration [43]. Differential charge densities were adopted to visually show charge density distribution in Fig. 1e ~ g. The extensive charge density around O-contained and Mn sites could be obviously observed, while it was less visible in the model of –F terminal $Ti_3C_2T_x$, indicating that the Mn ions were inclined to couple with O-contained terminal. In particular, the different binding energies showed a lowest value of −8.728 eV of Mn–OH bond in Table S1, further proving the trend that Mn ions preferred to form bond with –OH terminal.

Understanding what happened after cation intercalation in $Ti_3C_2T_x$, we mainly pay attention to the performance enhancement of interspace engineering material. The morphologies were examined by scanning electron microscopy (SEM), transmission electron microscopy (TEM), and atomic force microscopy (AFM) techniques. The raw $Ti_3C_2T_x$ nanosheets showed a size of ~200 nm (Fig. 2a) and these nanosheets were inclined to a tight restack. Fig. 2b exhibited a $Ti_3C_2T_x$ film, where the little dots at the edges of the flakes are titanium dioxide due to the surface exposure to air. Compared with the $Ti_3C_2T_x$ film, the MIT film in Fig. 2c displayed smooth surface, and the cross-section SEM images (Fig. S2c) exhibited a lamellar structure. Additionally, the thickness of MIT nanosheets were about 3.46 nm (Fig. 2h). The element mapping of the vertical-view image (Fig. 2g) showed that the Ti, C, O, F, and Mn elements were homogeneously dispersed in the hybrid film, indicating that Mn ions were successfully intercalated into the interlayer of negatively charged $Ti_3C_2T_x$.

$Ti_3C_2T_x$ nanosheets were shown in Fig. 2d, where the bottom left inset displayed the high-resolution TEM (HRTEM) images of $Ti_3C_2T_x$ nanosheets, corresponding to a clear adjacent lattice fringe of 0.27 nm. Fig. 2e showed a d-spacing of ≈1.3 nm in the raw $Ti_3C_2T_x$ nanosheets, while the introduced Mn ions caused an increased two-layer d-spacing of 3.2 nm in Fig. 2f, suggesting that the single interlayer spacing was 1.6 nm. The observed difference of 0.3 nm was larger than the diameter of Mn ions (0.134 nm), maybe owing to the insertion of a solvent molecule and the bond formation [44], which was consistent with the simulating calculation results. The expanded interlayer spacing is beneficial for the intercalation of electrolyte ions into layers of electrode materials during the electrochemical process.

The Raman spectra of the raw $Ti_3C_2T_x$ film and MIT films were characterized and depicted in Fig. 3a. The two lines displayed the typical signatures of $Ti_3C_2T_x$ MXene, in agreement with the literature [45]. Specifically, both lines exhibited strong peak at 201 cm^{-1}, which was assigned to the A_{1g} modes of $Ti_3C_2O_2$. Moreover, the modes at 383, 576, and 725 cm^{-1} were originated from the vibrations of C atoms in $Ti_3C_2O_2$. The peak at 441 cm^{-1} was attributed to the vibrations of atoms in $Ti_3C_2(OH)_2$, while that at 622 cm^{-1} was assigned to the E_g of $Ti_3C_2F_2$. Apparently, the additional peak at 150 cm^{-1} in MIT film as the signature of A_{1g} symmetry out-of-plane vibrations of the $Ti_3C_2T_x$ bond, indicative of the expansion in the c-direction caused by the intercalation between the $Ti_3C_2T_x$ nanosheets [46].

X-ray photoelectron spectroscopy (XPS) was conducted to analyze the bond formation and elements' valence in change. The survey spectrum in Fig. 3b clearly revealed an additive Mn 2p peak with a red line, indicating that Mn ions were successively intercalated into $Ti_3C_2T_x$. A similar Ti 2p level displayed in the two lines of Fig. 3c was fitted with three doublets corresponding to Ti $2p_{3/2}$ and Ti $2p_{1/2}$. The first doublet at 453.3 and 457.72 eV, the second doublet at 454.0 and 459.5 eV, and the third doublet at 455.2 and 460.6 eV were assigned to Ti–C, Ti^{2+}, and Ti–O of $Ti_3C_2T_x$, respectively [47]. The C1s and F1s spectrums were shown in Fig. S3. F1s profile showed a peak of binding energy at 685.2 eV, indicating the C–Ti–F bond [47], and no additive peak/bond can be observed. In Fig. 3d, the O1s peak at 531.1 eV was corresponded to the Mn–O bond. These results were in agreement with the reliable DFT simulation. In addition, the high-resolution Mn 2p spectrum was shown in Fig. S3c, the two peaks two peaks located at 641.0 eV and 652.7 eV corresponded to Mn $2p_{3/2}$ and Mn $2p_{1/2}$ of divalent manganese ion (Mn (II)) [48,49]. Fig. 3e showed the XRD patterns of the raw $Ti_3C_2T_x$ film and MIT film. The position of the (002) peak was proportional to the c-lattice parameter, according to Bragg's equation [50]. Due to the insertion of cation, the (002) peak of $Ti_3C_2T_x$ shifted from 6.56° to 5.75°, in accordance with a increase in the interlayer spacing, further

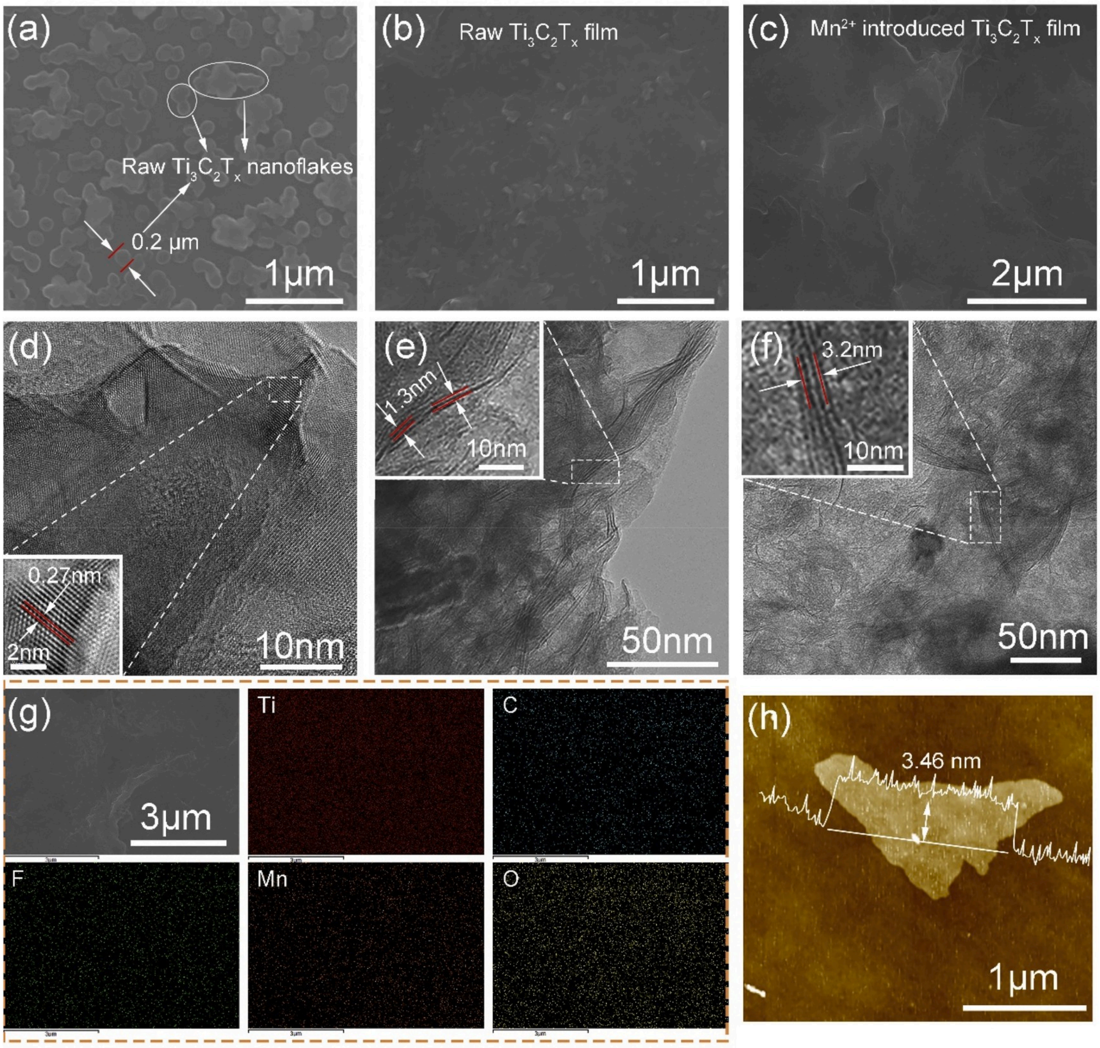

Fig. 2. (a–c) SEM images of (a) raw $Ti_3C_2T_x$ nanosheets, (b) raw $Ti_3C_2T_x$ films, and (c) MIT films. (d) HRTEM images of $Ti_3C_2T_x$ (inset image shows lattice fringes captured from the dashed square). (e,g) TEM images of (e) raw $Ti_3C_2T_x$ film, and (f) MIT films. (g) EDS of MIT. (h) AFM image and height profile of MIT.

demonstrating that cation intercalation led to the sufficient expansion of $Ti_3C_2T_x$ layers. In addition, the broadened diffraction peak suggested a slight loss in crystallinity, caused by structural distortion relevant with cation intercalation [30].

The electrochemical performance of as-fabricated MSCs based on MIT films and raw $Ti_3C_2T_x$ films was investigated by cyclic voltammetry (CV), galvanostatic charge–discharge (GCD), and electrochemical impedance spectroscopy (EIS) measurements. As shown in Fig. 4a, the CV curves of MIT-based MSCs ranging from 2 to 50 mV s^{-1} exhibited approximately quasi-rectangular shape within a voltage range of 0–1 V, reflecting a pseudocapacitive electrochemical characteristics, which performed as a reversible surface redox [51]. The intrinsic pseudocapacitance of $Ti_3C_2T_x$ could be attributed to that intercalated protons made reversible redox process with interfacial oxygen-containing group, and the valence change of Ti from $Ti_3C_2O_2$ converting to $Ti_3C_2O(OH)$ to realize the charge storage [16]. Besides, the partial pseudocapacitance had been contributed by the redox reaction of covalent-resembled Mn–O bonds, where the Mn element showed a higher valence compared with the bivalent [37]. The surface redox of Mn species could be expressed as following equation, where the MnO_a $(OH)_b$ and the MnO_{a-b} $(OH)_{b+\delta}$ represent the higher and lower oxidation states, respectively [52].

$$MnO_a(OH)_b + \delta H^+ + \delta e^- \leftrightarrow MnO_{a-b}(OH)_{b+\delta} \tag{1}$$

The analysis of charge storage kinetics were carried out based CV profiles, according to the relationship between peak current (I) and scan rate (υ) [53]:

$$i = av^b \tag{2}$$

where a and b are variables, the value of b is determined from the slope of the plot of log i versus log v, and it provides some information on the charge storage kinetics: b = 1 indicates fast ion diffusion with possibly capacitive/pseudocapacitive charging mechanism, while b = 0.5 associates with the diffusion limited processes [53,54]. According to this equation, the b-value evaluated was calculated as 0.75 in Fig. 4d, indicating that the charge storage was composed of the predominant contributions of capacitive, and diffusion-controlled processes due to bulk or inner effects [55].

To further quantify the capacitive and diffusion-limited contributions to the total capacitance, the following relationship was performed according to previous reports:

$$i(V) = k_1 v + k_2 v^{0.5} \tag{3}$$

where i (V) is the current at a given potential, k_1v and $k_2v^{0.5}$ correspond to the current contributions from the surface capacitive effect and the diffusion-controlled intercalation process, respectively [53,54]. By finding the common values, we quantified the fraction of the current (proportional to capacitance) originating from the capacitive and

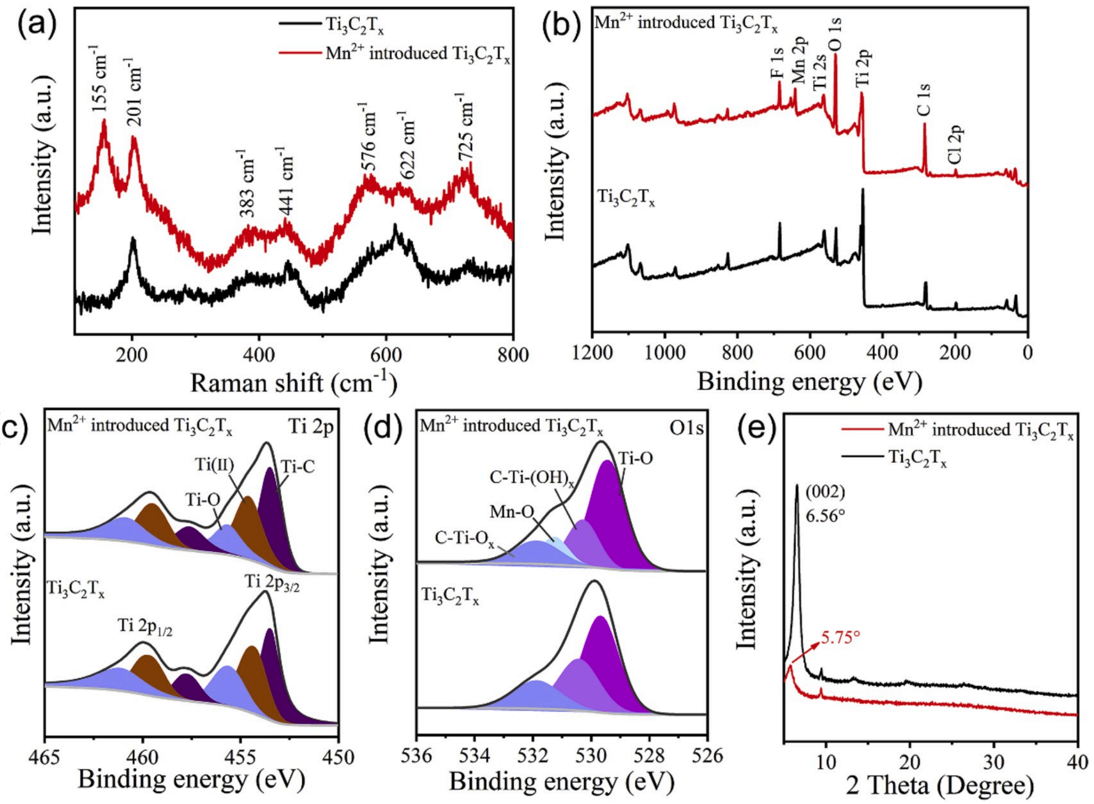

Fig. 3. Comparison of MIT (red line) and raw $Ti_3C_2T_x$ (black line). (a) Raman spectra, (b) XPS spectra, (c) high-resolution Ti 2p spectrum, (d) high-resolution O1s spectrum, and (e) XRD patterns.

diffusion-controlled processes. As displayed in Fig. 4e, the predominant contribution at 5 mV s^{-1} came from the surface capacitive effect, which occupied 90.2% of the total capacitance, confirming that the mechanism of charge storage of MIT-based MSCs was predominantly pseudocapacitive.

For comparison, the CV curves of raw $Ti_3C_2T_x$ -based MSCs from 2 to 100 mV s^{-1} were shown in Fig. 4b, where the slanted shape presented that the MSCs summitted a more resistive behavior, attributable to the poor electroconductivity and ohmic contact resistance between flakes. The asymmetric CVs of $Ti_3C_2T_x$ MSCs occurred with increasing of scan rate, while the CV loops of MIT-based MSCs delivered a symmetric and stable feature, confirming the electrochemical reversibility and stability improvement of MSCs after Mn ions intercalation. The GCD profiles of MIT-based MSCs showed nearly isosceles triangle shapes at a current density of 0.1–0.3 mA cm^{-2} (Fig. 4c), further implying its great capacitive performance. Compared to the GCD curves of $Ti_3C_2T_x$ MSCs in Fig. S4a, a longer discharge time of MIT-based MSCs at the same current density indicated enhanced electrochemical performance. Fig. S4b compared the capacitances of two types of MSCs. The MIT-based MSCs displayed excellent rate capability and acquired the maximum areal capacitance of ~87 mF cm^{-2} at a scan rate of 2 mV s^{-1}, while raw $Ti_3C_2T_x$-based MSCs delivered a small capacitance of 77.5 mF cm^{-2} at the same scan rate, which was ascribed to inferior conductivity (shown in Fig. 5d). Compared with the raw $Ti_3C_2T_x$-based MSCs, an increased capacitance ratio of 18% in MIT-based MSCs can be obtained at the smaller scan rate in Fig. S4b, which can be attributed to the expanded interspace of $Ti_3C_2T_x$ exposing more active sites for redox reaction and partial pseuocapacitance provided by interfacial redox of Mn–O bonds. Here the slight capacitance improvement after cation intercalation is not attractive, which can be relevant with the following aspects. The unfavorable titanium dioxide was formed at the edges of $Ti_3C_2T_x$ flake because the surface was exposed in air [56], which passivated the material surface and hindered the surface redox reaction during charge-discharge process. On the other hand, the anodic $Ti_3C_2T_x$-based electrodes in interdigital MSCs were oxidized at positive (anodic) potential [57], causing an irreversible capacitance loss. Electrochemical impedance spectroscopy (EIS) was performed to measure the impedance of MSCs as a function of frequency. The point intersecting the real axis of the impedance in Fig. 4f showed the equivalent series resistance (ESR) originating from the total internal resistance of the cell (an additive effect from the cell components and electrolytes), where the MIT-based MSCs had a smaller value of 133.4 Ω compared with that of raw $Ti_3C_2T_x$-based MSCs. Besides, a larger 79.1° angle line with respect to the real axis of impedance could be observed in MIT-based MSCs, meaning that pseudocapacitive is predominant. Limited diffusion could contribute to the lower angle value of raw $Ti_3C_2T_x$-based MSCs.

To further demonstrate the excellent energy storage ability, the Ragone plot of the MIT-based MSCs in this study was given in comparison with those of other currently reported MXene based MSCs (Fig. 4g and Table S5). Remarkably, the highest volumetric energy density was reached up to 11.8 mWh cm^{-3} at a power density of 100.8 mW cm^{-3}, which was comparable with other micro-supercapacitors based few-layered MXene flakes (6.35–7.48 mWh cm^{-3}) [58], sprayable MXene conductive inks (1.48 mWh cm^{-3} at a power density of 189.9 mW cm^{-3}) [59], few-layered $Ti_3C_2T_x$ nanosheets (2.3 mWh cm^{-3} at a power density of 159.6 mW cm^{-3}) [60]. Note that the capacitance and energy density are still need to improve in order to meet the increasing energy demands of micro electronic devices and systems. Besides, we also constructed the integrated MSCs pack connected in parallel and in series to satisfy the different demands. As expected, the integration area of the CV loop, associated with the capacitance, was enlarged by connecting two MSCs units in parallel (Fig. 4h), and GCD profile displayed a discharge time of about two times that of a single MSC, indicating a double growth of the capacitance. In a serial structure, the integrated MSCs exhibited a progressive voltage extension of 2 V, as observed from the voltage windows from both CV and GCD curves (Fig. 4h–i).

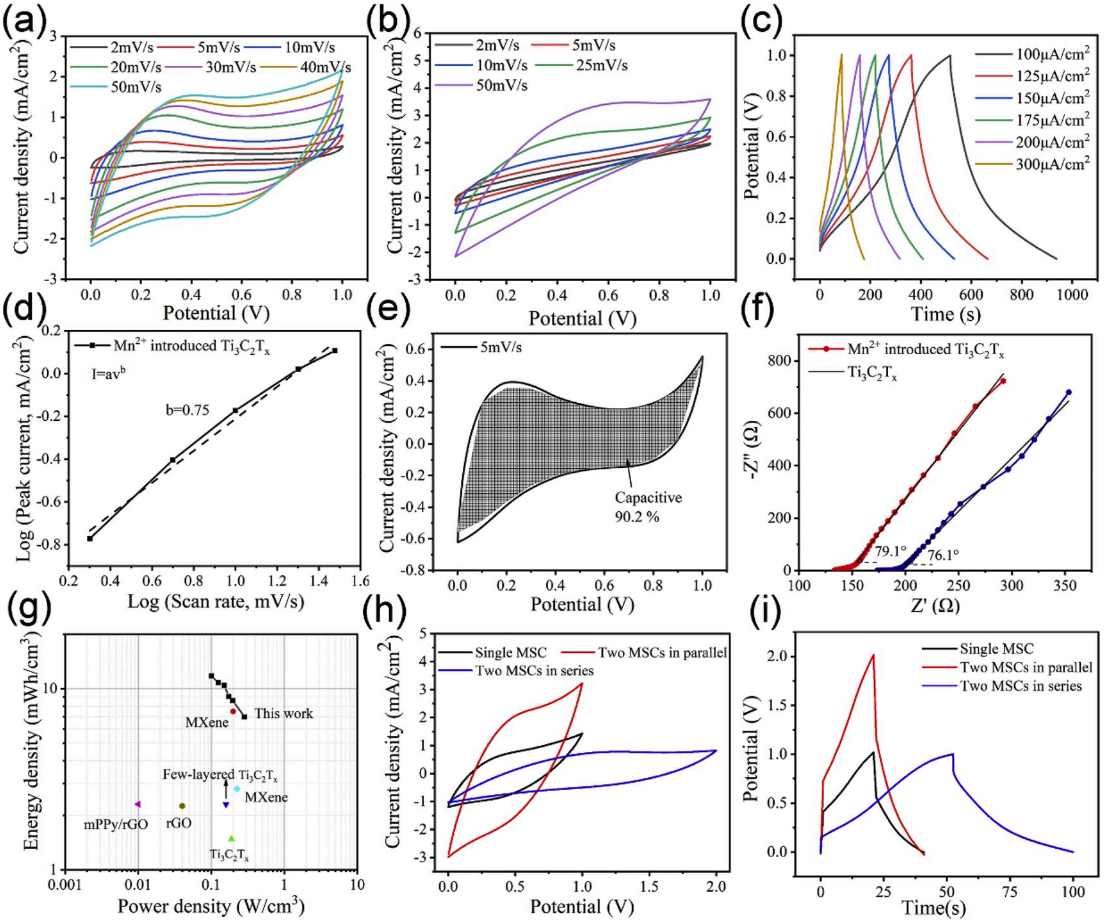

Fig. 4. Electrochemical performances of $Ti_3C_2T_x$ MXene-based MSCs in PVA/H_3PO_4 gel electrolyte. (a) CV curves of MIT-based MSCs. (b) CV curves of raw $Ti_3C_2T_x$-based MSCs, (c) GCD profiles of MIT-based MSCs. (d) b-values of MIT-based MSCs, calculated from the anodic peak current value at the scan rate range of 2–30 mV/s, (e) Cyclic voltammetry profiles of MIT-based MSCs at 5 mV/s with hatched portions corresponding to the current contributions from the surface capacitive. (f) Nyquist plots (red line presents MIT-based MSCs, black line indicates raw $Ti_3C_2T_x$-based MSCs), (g) Ragone plot of MIT-based MSCs (based on the GCD profiles). (h) CV curves tested at 80 mV s^{-1}, and (i) GCD profiles measured at 0.75 mA cm^{-2} of MIT-based MSCs connected in series or in parallel.

The flexible MIT-based MSCs were further subjected to mechanical bending tests (Fig. 5a), and their CV curves were plotted in Fig. 5b. It was observed that the CV curves expanded in the convex states, indicating the capacitance enhancement at convex bending states. When the MSC was in the concave states, the CV lines showed no obvious changes, demonstrative of excellent flexibility and electrochemical stability. Fig. 5c presented the cyclic stability of MIT-based MSCs. Evidently, 82% capacitance retention could be readily achieved after 5000 cycles at a scan rate of 100 mV s^{-1}.

Based on the as-prepared $Ti_3C_2T_x$ materials, the EMI shielding efficiency (SE) was investigated at the X-band (8.2–12.4 GHz). Note that the electrical conductivity is an important factor for EMI shielding [28]. As shown in Fig. 5d, the MIT films exhibited an average electrical conductivity of 4268 S m^{-1}, which was more than two times that of the pristine $Ti_3C_2T_x$ films (1894 S m^{-1}), enabled the fast transport of electrons. This is because the cation acted as a link to connect the $Ti_3C_2T_x$ nanosheets. The measured SE_R, SE_A, and SE_T were illustrated in Fig. 5e–f and Fig. S5a-b. Compared to the raw $Ti_3C_2T_x$ film, the MIT films displayed a high average SE_T value of 44.3 dB with a thickness of 2.5 μm (Fig. S2b), while the raw $Ti_3C_2T_x$ film maintained a stable value of only 24.1 dB. Moreover, MIT film also exhibited a highest SE of 69 dB at 9.4 GHz.

For Mxenes, the absorption, reflection, and multilayer internal reflection are the main ways to attenuate electromagnetic waves [28]. In this work, it was noted that the MIT films and raw $Ti_3C_2T_x$ films exhibited similar reflection loss (SE_R, Fig. 5f), but the former value of SE_A was over two times that of the pure film, implying that absorption, especially the additive internal absorption, caused energy loss of electromagnetic waves. The absorbed EM wave dissipated mainly in the form of heat energy caused by available electron migration, in agreement with the enhancement of conductivity [61]. The mechanism of electromagnetic wave action in MIT film is vividly depicted in Fig. 1. Compared to other MXene-based thin films, such as f-Ti_2CT_x/PVA film with an SE of 21/26 dB [28] and $Ti_3C_2T_x$/TOCNF composite films with an SE of 39.6 dB [62], the results of our study show a more competitive EMI shielding performance.

3. Conclusion

In summary, a highly conductive Mn ions introduced $Ti_3C_2T_x$ MXene was developed as a promising material for MSCs functional EMI shielding. The cation intercalation mechanism of $Ti_3C_2T_x$ was explored as that Mn ions were inclined to be bonding with interfacial oxygen-contained terminal, performed as the orbital hybridization of Mn 3d and O 2p. Cation intercalation enabled to expand the d-space and improve the electrical conductivity of $Ti_3C_2T_x$. With the unrivaled features of Mn ions-introduced $Ti_3C_2T_x$, the as-prepared MSCs delivered excellent energy storage ability and outstanding EMI shielding efficiency. This study can provide powerful information on the surface structure and the intercalation mechanism of $Ti_3C_2T_x$ at the atomic level, enrich the understanding of interlayer engineering of the MXenes. More importantly, this work also can propose new views of functional

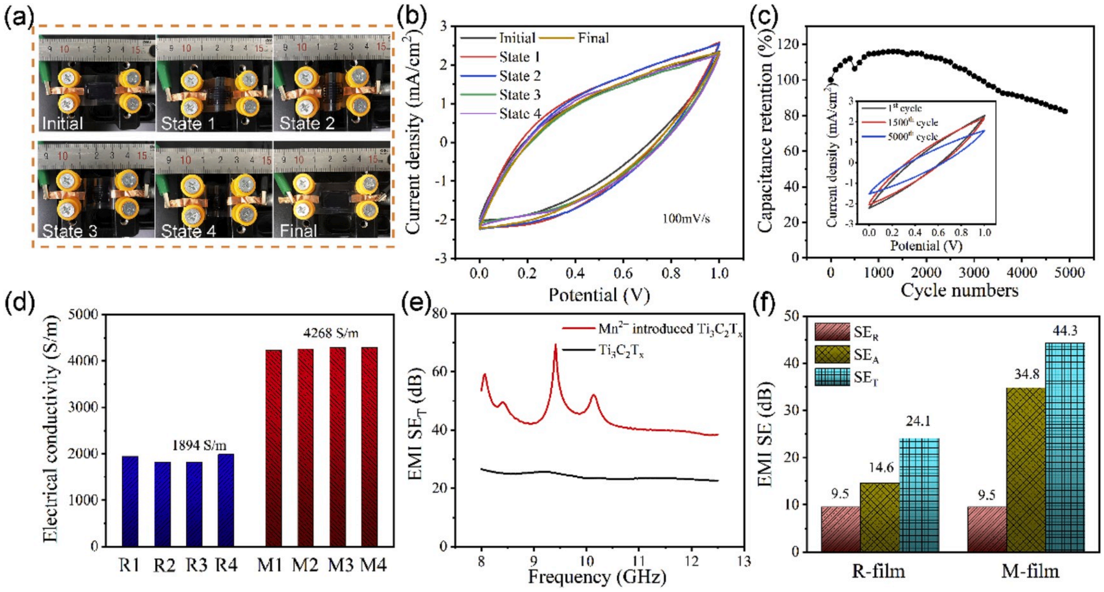

Fig. 5. (a) Photographs and (b) CV curves of MIT-based MSCs under various bending states (states 1–2 represent Δ = 5 and 10 mm (convex) and states 3–4 represent Δ = 5 and 10 mm (concave)).The gray line indicates the initial state, the red and blue lines indicate different convex states and. (c) Cycling stability obtained at a scan rate of 100 mV s^{-1}. (d) Electrical conductivities of raw $Ti_3C_2T_x$ films (measured four samples and named as R1–4) and MIT films (measured four samples and named as M1–4). (e) SE_T, EMI shielding performances of raw $Ti_3C_2T_x$ film and MIT film at X-band. (f) Proportion of reflection (SE_R), absorption (SE_A), and total EMI SE (SE_T) of raw $Ti_3C_2T_x$ film and MIT film.

MSCs with EMI shielding for special on-chip application in microelectronics, endowing great significance for the stability of integrated circuits and micro-systems.

4. Methods

Materials: The $Ti_3C_2T_x$ nanosheets were obtained from 11 Technology Co., Ltd. (JiLin, China), and introduced by the "LiF + HCl" etching method from Ti_3AlC_2 MAX.

Preparation of Mn ions-introduced $Ti_3C_2T_x$ suspension: 2 mL of $MnCl_2$ solution (10 mmol L^{-1}) was added into 50 mL $Ti_3C_2T_x$ MXene suspension (1 mg mL^{-1}). Next, the $Ti_3C_2T_x$ MXene suspension flocculated with Mn^{2+} was formed within a few seconds. The mixture suspension was also sonicated for 2 h to obtain homogeneous Mn^{2+}-introduced $Ti_3C_2T_x$ nanosheets.

Fabrication of flexible all-solid-state MSCs: The MSCs were directly manufactured through mask-assisted filtration of $Ti_3C_2T_x$ MXene suspension. Then, the MSCs obtained by vacuum filtration were readily dry-transferred onto a flexible PET substrate (Fig. 1g), without the need of metal-based current collectors. The average mass loading of MIT-based MSCs and raw $Ti_3C_2T_x$-based MSCs were weighed to be 1.75 mg and 1.66 mg, respectively (shown in Table S3). Finally, the as-prepared MSCs were poured into a PVA/H_3PO_4 gel electrolyte and left to stand for several minutes to solidify the gel electrolyte, thereby producing the flexible all-solid-state MSCs.

Characterizations: The microstructure and morphology of the electrode materials were characterized with SEM (Quanta 600FEG, FEI, USA), a Bruker multimode 8 atomic force microscope, and a transmission electron microscope (FEI Talos F200X). The crystallinity of the composite was evaluated by a high-resolution XRD (D8 Discovery, Bruker, Germany) analysis in the Bragg (reflection) geometry with pure Cu kα1 radiation (wavelength; λ; 1.54056 Å). The Raman spectrum was investigated with a Raman spectroscopy system (Lab Ram HR 800, Horiba JY, Japan), by using an Ar^+ laser (wavelength of 414 nm) as the excitation source. The elemental analysis of the composite was conducted by XPS (ESCALAB, 250Xi, Thermo Fisher Scientific, USA). The electrical conductivity values of the samples were measured using a four-point probe instrument (FT-341 serial resistivity tester) at room temperature.

Electrochemical testing was performed on a CHI660E electrochemical workstation (CH Instruments China) in a two-electrode system. The cyclic voltammetry (CV), galvanostatic charge/discharge (GCD or It) and electrochemical impedance spectra (EIS) were measured and analyzed. EIS was performed in the frequency range of 0.01 Hz–100 kHz at an open-circuit voltage with an amplitude of 5 mV. Parametric calculations for MSCs are discussed in detail in Support information.

An Anritsu MS46322A series vector network analyzer was employed to analyze the EMI shielding performance of Mxene films in the frequency range of 8.2–12.4 GHz (X-band), by using the coaxial flange method. The detailed description and calculation were depicted in Support information.

DFT Simulation: DFT was employed to study the interaction mechanism between Mn^{2+} and surface functional groups of $Ti_3C_2T_x$ MXene with the pseudopotential plane-wave method implemented in the Cambridge Sequential Total Energy Package (CASTEP). The exchange-correlation potential was described by the Perdew–Burke–Ernzerhof function with the generalized gradient approximation. The plane-wave energy cutoff was set to 400 eV, and the Monkhorst-Pack method with G-centered 9 × 9 × 1 K-point mesh was used for the Brillouin zone. The convergence criteria of energy and force calculations were set to 5.0 e^{-6} eV per atom and 0.01 eV/Å. To avoid spurious interactions between the periodic images, a vacuum space of 20 Å was used.

Declaration of competing interest

The authors declare that they have no known competing financial interests or personal relationships that could have appeared to influence the work reported in this paper.

Acknowledgments

The work was supported by the National Natural Science Foundation of China (Grant No. 61334002, 51872283, and 21805273), the Natural Science Basic Research Plan in Shaanxi Province of China (Program No.2016ZDJC-09), Young Talent fund of University Association for

Science and Technology in Shaanxi, China (Program No.201701060), the Wuhu and Xidian University special fund for industry- university-research cooperation, China (Program No.HX01201909039), Natural Science Basic Research Plan in Shaanxi Province of China (Program No. 2019JQ-860), the Fundamental Research Funds for the Central Universities of China, the Innovation Fund of Xidian University of China, Natural Science Foundation of Liaoning Province, Joint Research Fund Liaoning-Shenyang National Laboratory for Materials Science (Grant 20180510038), LiaoNing Revitalization Talents Program (Grant XLYC1807153), DICP (DICP ZZBS201708, DICP ZZBS201802), Dalian National Laboratory For Clean Energy (DNL), CAS, DICP&QIBEBT (Grant DICP&QIBEBT UN201702), DNL Cooperation Fund, CAS (DNL180310, DNL180308, DNL201912, and DNL201915).

Appendix A. Supplementary data

Supplementary data to this article can be found online at https://doi.org/10.1016/j.nanoen.2020.104741.

References

[1] H. Guo, X.P. Pu, J. Chen, Y. Meng, M.-H. Yeh, G. Liu, Q. Tang, B. Chen, D. Liu, S. Qi, C. Wu, C. Hu, J. Wang, Z.L. Wang, A highly sensitive, self-powered triboelectric auditory sensor for social robotics and hearing aids, Science Robotics 3 (2018).

[2] S. Xu, W. Liu, B. Hu, X. Wang, Circuit-integratable high-frequency micro supercapacitors with filter/oscillator demonstrations, Nanomater. Energy 58 (2019) 803–810.

[3] J. Yun, C. Song, H. Lee, H. Park, Y.R. Jeong, J.W. Kim, S.W. Jin, S.Y. Oh, L. Sun, G. Zi, J.S. Ha, Stretchable array of high-performance microsupercapacitors charged with solar cells for wireless powering of an integrated strain sensor, Nanomater. Energy 49 (2018) 644–654.

[4] Q. Jiang, C. Wu, Z. Wang, A.C. Wang, J.-H. He, Z.L. Wang, H.N. Alshareef, MXene electrochemical microsupercapacitor integrated with triboelectric nanogenerator as a wearable self-charging power unit, Nanomater. Energy 45 (2018) 266–272.

[5] J. Cai, C. Lv, A. Watanabe, Laser direct writing and selective metallization of metallic circuits for integrated wireless devices, ACS Appl. Mater. Interfaces 10 (2017) 915–924.

[6] Y. Yue, Z. Yang, N. Liu, W. Liu, H. Zhang, Y. Ma, C. Yang, J. Su, L. Li, F. Long, Z. Zou, Y. Gao, A flexible integrated system containing a microsupercapacitor, a photodetector, and a wireless charging coil, ACS Nano 10 (2016) 11249–11257.

[7] D. Kim, D. Kim, H. Lee, Y.R. Jeong, S.J. Lee, G. Yang, H. Kim, G. Lee, S. Jeon, G. Zi, J. Kim, J.S. Ha, Body-attachable and stretchable multisensors integrated with wirelessly rechargeable energy storage devices, Adv. Mater. 28 (2016) 748–756.

[8] X. Shi, S. Zheng, Z.-S. Wu, X. Bao, Recent advances of graphene-based materials for high-performance and new-concept supercapacitors, Journal of Energy Chemistry 27 (2018) 25–42.

[9] Y. Da, J. Liu, L. Zhou, X. Zhu, X. Chen, L. Fu, Engineering 2D architectures toward high-performance micro-supercapacitors, Adv. Mater. 31 (2019), e1802793.

[10] N. Liu, Y. Gao, Recent progress in micro-supercapacitors with in-plane interdigital electrode architecture, Small 13 (2017).

[11] X. Feng, J. Ning, D. Wang, J. Zhang, J. Dong, C. Zhang, X. Shen, Y. Hao, All-solid-state planner micro-supercapacitor based on graphene/NiOOH/Ni(OH)2 via mask-free patterning strategy, J. Power Sources 418 (2019) 130–137.

[12] X. Wang, Q. Zhang, On-chip microsupercapacitors: from material to fabrication, Energy Technol. 7 (2019).

[13] S. Gupta, N.-H. Tai, Carbon materials and their composites for electromagnetic interference shielding effectiveness in X-band, Carbon 152 (2019) 159–187.

[14] D. Jiang, V. Murugadoss, Y. Wang, J. Lin, T. Ding, Z. Wang, Q. Shao, C. Wang, H. Liu, N. Lu, R. Wei, A. Subramania, Z. Guo, Electromagnetic interference shielding polymers and nanocomposites - a review, Polym. Rev. 59 (2019) 280–337.

[15] P.M. Mariappan, D.R. Raghavan, S.H.E.A. Aleem, A.F. Zobaa, Effects of electromagnetic interference on the functional usage of medical equipment by 2G/3G/4G cellular phones: a review, J. Adv. Res. 7 (2016) 727–738.

[16] B. Anasori, M.R. Lukatskaya, Y. Gogotsi, 2D metal carbides and nitrides (MXenes) for energy storage, Nature Reviews Materials 2 (2017).

[17] J. Nan, X. Guo, J. Xiao, X. Li, W. Chen, W. Wu, H. Liu, Y. Wang, M. Wu, G. Wang, Nanoengineering of 2D MXene-based materials for energy storage applications, Small (2019), e1902085.

[18] Y.-Y. Peng, B. Akuzum, N. Kurra, M.-Q. Zhao, M. Alhabeb, B. Anasori, E.C. Kumbur, H.N. Alshareef, M.-D. Ger, Y. Gogotsi, All-MXene (2D titanium carbide) solid-state microsupercapacitors for on-chip energy storage, Energy Environ. Sci. 9 (2016) 2847–2854.

[19] X. Zhan, C. Si, J. Zhou, Z. Sun, MXene and MXene-based composites: synthesis, properties and environment-related applications, Nanoscale Horizons 5 (2020) 235–258.

[20] M. Naguib, M. Kurtoglu, V. Presser, J. Lu, J. Niu, M. Heon, L. Hultman, Y. Gogotsi, M.W. Barsoum, Two-dimensional nanocrystals produced by exfoliation of Ti3 AlC2, Adv. Mater. 23 (2011) 4248–4253.

[21] O.M. Michael Naguib, Joshua Carle, Volker Presser, Jun Lu, Lars Hultman, Yury Gogotsi, Michel W. Barsoum, Two-dimensional transition metal carbides, ACS Nano 6 (2012) 1322–1331.

[22] Y. Xia, T.S. Mathis, M.Q. Zhao, B. Anasori, A. Dang, Z. Zhou, H. Cho, Y. Gogotsi, S. Yang, Thickness-independent capacitance of vertically aligned liquid-crystalline MXenes, Nature 557 (2018) 409–412.

[23] L. Yu, Z. Fan, Y. Shao, Z. Tian, J. Sun, Z. Liu, Versatile N-doped MXene ink for printed electrochemical energy storage application, Advanced Energy Materials 9 (2019).

[24] X. Zang, C. Jian, T. Zhu, Z. Fan, W. Wang, M. Wei, B. Li, M. Follmar Diaz, P. Ashby, Z. Lu, Y. Chu, Z. Wang, X. Ding, Y. Xie, J. Chen, J.N. Hohman, M. Sanghadasa, J. C. Grossman, L. Lin, Laser-sculptured ultrathin transition metal carbide layers for energy storage and energy harvesting applications, Nat. Commun. 10 (2019) 3112.

[25] C.J. Zhang, L. McKeon, M.P. Kremer, S.H. Park, O. Ronan, A. Seral-Ascaso, S. Barwich, C.O. Coileain, N. McEvoy, H.C. Nerl, B. Anasori, J.N. Coleman, Y. Gogotsi, V. Nicolosi, Additive-free MXene inks and direct printing of micro-supercapacitors, Nat. Commun. 10 (2019) 1795.

[26] G.-M. Weng, J. Li, M. Alhabeb, C. Karpovich, H. Wang, J. Lipton, K. Maleski, J. Kong, E. Shaulsky, M. Elimelech, Y. Gogotsi, A.D. Taylor, Layer-by-Layer assembly of cross-functional semi-transparent MXene-carbon nanotubes composite films for next-generation electromagnetic interference shielding, Adv. Funct. Mater. 28 (2018).

[27] M.-S. Cao, Y.-Z. Cai, P. He, J.-C. Shu, W.-Q. Cao, J. Yuan, 2D MXenes: electromagnetic property for microwave absorption and electromagnetic interference shielding, Chem. Eng. J. 359 (2019) 1265–1302.

[28] M.A.F. Shahzad, C.B. Hatter, B. Anasori, S. Man Hong, Y.G.C.M. Koo, Electromagnetic interference shielding with 2D transition metal carbides (MXenes), Science (2016) 353.

[29] J.L. Hart, K. Hantanasirisakul, A.C. Lang, B. Anasori, D. Pinto, Y. Pivak, J.T. van Omme, S.J. May, Y. Gogotsi, M.L. Taheri, Control of MXenes' electronic properties through termination and intercalation, Nat. Commun. 10 (2019) 522.

[30] C. Wang, S. Chen, H. Xie, S. Wei, C. Wu, L. Song, Atomic Sn4+Decorated into vanadium carbide MXene interlayers for superior lithium storage, Advanced Energy Materials 9 (2019).

[31] P. Lian, Y. Dong, Z.-S. Wu, S. Zheng, X. Wang, W. Sen, C. Sun, J. Qin, X. Shi, X. Bao, Alkalized Ti3C2 MXene nanoribbons with expanded interlayer spacing for high-capacity sodium and potassium ion batteries, Nanomater. Energy 40 (2017) 1–8.

[32] M. Hu, R. Cheng, Z. Li, T. Hu, H. Zhang, C. Shi, J. Yang, C. Cui, C. Zhang, H. Wang, B. Fan, X. Wang, Q.-H. Yang, Interlayer engineering of Ti3C2Tx MXenes towards high capacitance supercapacitors, Nanoscale 12 (2020) 763–771.

[33] J. Li, X. Yuan, C. Lin, Y. Yang, L. Xu, X. Du, J. Xie, J. Lin, J. Sun, Achieving high pseudocapacitance of 2D titanium carbide (MXene) by cation intercalation and surface modification, Advanced Energy Materials 7 (2017).

[34] H. Yu, Y. Wang, Y. Jing, J. Ma, C.F. Du, Q. Yan, Surface modified MXene-based nanocomposites for electrochemical energy conversion and storage, Small 15 (2019), e1901503.

[35] K. Hantanasirisakul, Y. Gogotsi, Electronic and optical properties of 2D transition metal carbides and nitrides (MXenes), Adv. Mater. 30 (2018), e1804779.

[36] M. Naguib, Y. Gogotsi, Synthesis of two-dimensional materials by selective extraction, Acc. Chem. Res. 48 (2015) 128–135.

[37] C. Wang, H. Xie, S. Chen, B. Ge, D. Liu, C. Wu, W. Xu, W. Chu, G. Babu, P. M. Ajayan, L. Song, Atomic cobalt covalently engineered interlayers for superior lithium-ion storage, Adv. Mater. 30 (2018), e1802525.

[38] C. Zhan, T. Wu, J. Lu, K. Amine, Dissolution, migration, and deposition of transition metal ions in Li-ion batteries exemplified by Mn-based cathodes – a critical review, Energy Environ. Sci. 11 (2018) 243–257.

[39] H. Chu, F. Zhang, L. Pei, Z. Cui, J. Shen, M. Ye, Ni, Co and Mn doped SnS2-graphene aerogels for supercapacitors, J. Alloys Compd. 767 (2018) 583–591.

[40] L. Li, Lattice dynamics and electronic structures of Ti3C2O2 and Mo2TiC2O2 (MXenes): the effect of Mo substitution, Comput. Mater. Sci. (2016) 8–14.

[41] H.A. Tahini, X. Tan, S.C. Smith, The origin of low workfunctions in OH terminated MXenes, Nanoscale 9 (2017) 7016–7020.

[42] M. Khazaei, A. Ranjbar, M. Ghorbani-Asl, M. Arai, T. Sasaki, Y. Liang, S. Yunoki, Nearly free electron states in MXenes, Phys. Rev. B (2016) 93.

[43] J. Wen, X. Zhang, H. Gao, Role of the H-containing groups on the structural dynamics of Ti 3 C 2 T x MXene, Phys. B Condens. Matter 537 (2018) 155–161.

[44] S. Park, K.-S. Lee, G. Bozoklu, W. Cai, S.T. Nguyen, R.S. Ruoff, Graphene Oxide Papers Modified by Divalent Ions—Enhancing Mechanical Properties via Chemical Cross-Linking, ACS Nano 2 (2008) 572–578.

[45] T. Hu, J. Wang, H. Zhang, Z. Li, M. Hu, X. Wang, Vibrational properties of Ti3C2 and Ti3C2T2 (T = O, F, OH) monosheets by first-principles calculations: a comparative study, Phys. Chem. Chem. Phys. 17 (2015) 9997–10003.

[46] W. Feng, H. Luo, Y. Wang, S. Zeng, Y. Tan, L. Deng, X. Zhou, H. Zhang, S. Peng, Mxenes derived laminated and magnetic composites with excellent microwave absorbing performance, Sci. Rep. 9 (2019) 3957.

[47] W. Zhao, J. Peng, W. Wang, B. Jin, T. Chen, S. Liu, Q. Zhao, W. Huang, Interlayer hydrogen-bonded metal porphyrin frameworks/MXene hybrid film with high capacitance for flexible all-solid-state supercapacitors, Small 15 (2019), e1901351.

[48] A. Moses Ezhil Raj, S.G. Victoria, V.B. Jothy, C. Ravidhas, J. Wollschläger, M. Suendorf, M. Neumann, M. Jayachandran, C. Sanjeeviraja, XRD and XPS characterization of mixed valence Mn3O4 hausmannite thin films prepared by chemical spray pyrolysis technique, Appl. Surf. Sci. 256 (2010) 2920–2926.

[49] Mei Yang, Yiren Zhong, Xianlong Zhou, Jingjing Ren, Liwei Su, Jinping Wei, Z. Zhou, Ultrasmall MnO@N-rich carbon nanosheets for high-power asymmetric supercapacitors, J. Mater. Chem. 2 (2014) 12519.

[50] X. Mu, D. Wang, F. Du, G. Chen, C. Wang, Y. Wei, Y. Gogotsi, Y. Gao, Y. Dall'Agnese, Revealing the pseudo-intercalation charge storage mechanism of MXenes in acidic electrolyte, Adv. Funct. Mater. 29 (2019).

[51] Y. Jiang, J. Liu, Definitions of pseudocapacitive materials: a brief review, Energy & Environmental Materials 2 (2019) 30–37.

[52] Q. Liao, N. Li, H. Cui, C. Wang, Vertically-aligned graphene@MnO nanosheets as binder-free high-performance electrochemical pseudocapacitor electrodes, J. Mater. Chem. 1 (2013).

[53] J.P.J. Wang, J. Lim, B. Dunn, Pseudocapacitive contributions to electrochemical energy storage in TiO2 (anatase) nanoparticles, J. Phys. Chem. C (2007) 14925–14931.

[54] M. Boota, C. Chen, K.L. Van Aken, J. Jiang, Y. Gogotsi, Organic-inorganic all-pseudocapacitive asymmetric energy storage devices, Nanomater. Energy 65 (2019).

[55] H. Shao, Z. Lin, K. Xu, P.-L. Taberna, P. Simon, Electrochemical study of pseudocapacitive behavior of Ti3C2Tx MXene material in aqueous electrolytes, Energy Storage Materials 18 (2019) 456–461.

[56] A. Lipatov, M. Alhabeb, M.R. Lukatskaya, A. Boson, Y. Gogotsi, A. Sinitskii, Effect of synthesis on quality, electronic properties and environmental stability of individual monolayer Ti3C2MXene flakes, Advanced Electronic Materials 2 (2016).

[57] K. Li, X. Wang, S. Li, P. Urbankowski, J. Li, Y. Xu, Y. Gogotsi, An ultrafast conducting Polymer@MXene positive electrode with high volumetric capacitance for advanced asymmetric supercapacitors, Small 16 (2020), e1906851.

[58] H. Hu, Z. Bai, B. Niu, M. Wu, T. Hua, Binder-free bonding of modularized MXene thin films into thick film electrodes for on-chip micro-supercapacitors with enhanced areal performance metrics, J. Mater. Chem. 6 (2018) 14876–14884.

[59] H. Huang, X. Chu, H. Su, H. Zhang, Y. Xie, W. Deng, N. Chen, F. Liu, H. Zhang, B. Gu, W. Deng, W. Yang, Massively manufactured paper-based all-solid-state flexible micro-supercapacitors with sprayable MXene conductive inks, J. Power Sources 415 (2019) 1–7.

[60] P. Li, W. Shi, W. Liu, Y. Chen, X. Xu, S. Ye, R. Yin, L. Zhang, L. Xu, X. Cao, Fabrication of high-performance MXene-based all-solid-state flexible microsupercapacitor based on a facile scratch method, Nanotechnology 29 (2018) 445401.

[61] X. Li, W. You, L. Wang, J. Liu, Z. Wu, K. Pei, Y. Li, R. Che, Self-assembly-magnetized MXene avoid dual-agglomeration with enhanced interfaces for strong microwave absorption through a tunable electromagnetic property, ACS Appl. Mater. Interfaces 11 (2019) 44536–44544.

[62] Z. Zhan, Q. Song, Z. Zhou, C. Lu, Ultrastrong and conductive MXene/cellulose nanofiber films enhanced by hierarchical nano-architecture and interfacial interaction for flexible electromagnetic interference shielding, J. Mater. Chem. C 7 (2019) 9820–9829.